Pore-Scale Transport Resolved Model Incorporating Cathode Microstructure and Peroxide Growth in Lithium-Air Batteries

Charles P. Andersen,[a] Han Hu,[a] Gang Qiu,[a] Vibha Kalra,[b,*] and Ying Sun[a,z]

[a]*Department of Mechanical Engineering and Mechanics, Drexel University, Philadelphia, Pennsylvania 19104, USA*
[b]*Department of Chemical and Biological Engineering, Drexel University, Philadelphia, Pennsylvania 19104, USA*

The electrode microstructure plays an integral role in the performance of the non-aqueous Li-air battery. Computational modeling has proven to be an indispensible tool in the analysis of battery systems, but previous macroscale, volume-averaged models that consider the porous electrode as a homogenous medium of uniform geometric properties are insufficient to probe the effect of precise electrode microstructures. Utilizing a pore-scale transport-resolved model of the Li-air battery, the complex electrode and Li_2O_2 morphologies can be directly incorporated and their effects on the system-level performance can be evaluated. A thickness-dependent electrical conductivity of Li_2O_2 is considered in the model based on inputs from the density functional theory. Model validation is presented along with a sensitivity study of the applied current density and the reaction rate coefficient. The effect of electrode geometry (e.g., nanostructure spacing and height) on cell performance, including its influence on pore blocking compared against electrical insulation, is investigated. Pore blocking is observed for cathodes with nanostructure spacing less than twice a critical insulating thickness of Li_2O_2, suggesting the loss of active surface area as the mechanism for decreased cell performance. While for cathodes with larger nanostructure spacing, the discharge capacity is dictated by the electrical insulation of Li_2O_2.
 [DOI: 10.1149/2.0051507jes] All rights reserved.

Manuscript submitted January 15, 2015; revised manuscript received March 6, 2015. Published March 27, 2015.

Developing a battery with the energy density of fossil fuel has been an elusive goal that will likely usher in the widespread implementation of high-energy storage applications, such as electrified transportation[1]. Current Li-ion batteries (100 – 480 Wh $kg^{-1}_{practical}$[2–4]) have only 5–28% of the specific energy of gasoline (1700 Wh $kg^{-1}_{practical}$[5]); in order to drive 300 miles, an electric car would need a 500 kg Li-ion battery.[4] Alternatively, the non-aqueous Li-air (or more precisely Li-oxygen) batteries (1800 – 2700 Wh $kg^{-1}_{practical}$[6–10]) have up to 5 times the energy density of Li-ion batteries, putting them well within the range of gasoline[1]. Several factors contribute to the high energy density of Li-air battery: (i) there is no heavy transition metal in the cell,[11] (ii) lithium is the lightest and most electronegative anode metal, and (iii) the gaseous reactant O_2 is not contained within the cell but instead can be drawn from the surroundings. However, the relatively new Li-air battery still underperforms in several key factors when compared to the more established Li-ion battery, such as low round trip efficiency (70%[9,12] vs. >95%[13]), low drawing current density (0.1-1.0 mA cm^{-2}[8,14] vs. 30 mA cm^{-2}[14]) and poor cycle life (~100[15,16] vs. 5000[17]). The source of these problems can be traced to a number of key issues, including the electric insulation of the reaction products,[18–22] parasitic irreversible side reactions,[23–26] electrolyte instability,[12,23,24] and electrode degradation.[12,27] These shortcomings must be overcome in order for the Li-air battery to become viable.

Four primary variations of the Li-air battery has been studied in the literature, differentiated by the constitutive electrolyte: organic (non-aqueous), aqueous, hybrid organic/aqueous, and solid-state.[21] As shown schematically in Fig. 1, the non-aqueous Li-air battery consists of a lithium anode and a porous cathode submerged in an organic electrolyte. Its cathode is composed of high-surface area solid material (usually carbon) that forms an electrically conductive network and the overall cathode reaction is given by:[28]

$$2Li^+ + O_2 + 2e^- \leftrightarrow Li_2O_2 \qquad (2.96\,V) \qquad [1]$$

where the forward reaction is the oxygen reduction reaction (ORR) during discharge. As shown in Fig. 1, during discharge the low-solubility reaction products (e.g., Li_2O_2) deposit on the surface of the cathode material as solid precipitate that hinders charge transport to the electrode and reduces the available active surface area. Although parasitic side reactions may lead to the formation of Li_2CO_3 and other lithium alkyl carbonates,[23–25] Eq. 1 is the desired reversible reaction that ensures true rechargeability within the non-aqueous Li-air battery.[29] As such, the non-aqueous Li-air battery has received the most attention of the four configurations.[1]

The morphology of the Li_2O_2 formation significantly influences the performance of the non-aqueous Li-air battery. Although Li_2O_2 is the desired discharge product and essential for the oxygen evolution reaction (OER), it is also a bulk electrical insulator that impedes electronic transport and is believed to be the main cause of high overpotentials within Li-air batteries.[18–21] Using density functional theory calculations, Viswanathan et al.[22] showed that the conductivity of Li_2O_2 varies with its thickness and predicted the electron insulation at a Li_2O_2 film thickness between 5–10 nm. Based on this predicted insulation thickness, Xue et al.[30] developed a macroscale model for the electrode, featuring a pore size distribution with an expression for the probability of electron tunneling as a function of the film thickness. When the electron tunneling probability is small, the electrode becomes insulated. Recently, Hu et al.[31] showed that by decreasing the size of Li_2O_2 particles from 600 nm to 160 nm, a 230% increase

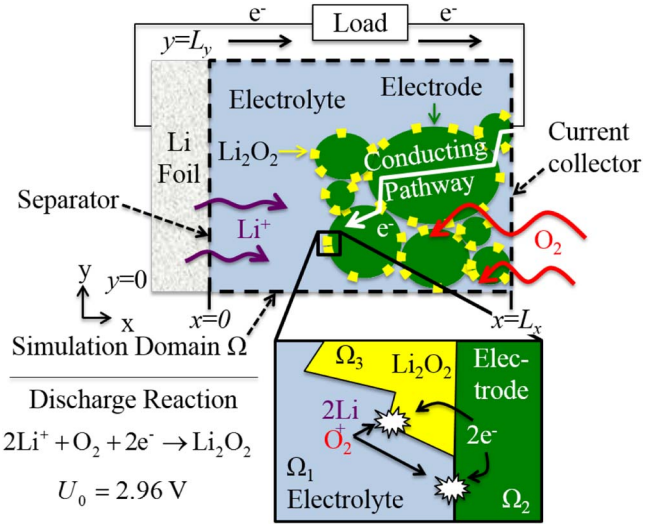

Fig. 1. Schematic of a non-aqueous Li-air battery. The microscale computational domain (Ω) consists of three distinct phases of electrolyte (Ω_1), electrode (Ω_2), and peroxide (Ω_3), which are mutually exclusive from another, i.e. $\Omega = \Omega_1 \cup \Omega_2 \cup \Omega_3$.

*Electrochemical Society Active Member.
zE-mail: YSun@coe.drexel.edu

in specific capacity, a 400 mV decrease in charging potential, and an 8% increase in round-trip efficiency are observed. Additionally, the complex electrode microstructure also plays a key role in determining the cell performance. The high-surface-area, porous electrodes are usually comprised of carbon-based materials that come in a variety of forms, including powders,[8] foams,[32] nanotubes[33] and nanofibers.[9] Although carbon electrodes have been shown to degrade during operation[7–9,12,23,27] (which has prompted the use of alternative more stable materials such as Au[16] and TiC[34]), the focus of this paper is on carbon-based electrodes. The electrodes in the Li-air cell both provide a site for the reactions to take place and help catalyze the ORR. Typically increasing the surface area of the electrode will improve the cell performance in terms of voltage and capacity. However, the discharge capacity also relates closely to the electrode pore size,[35] because the Li_2O_2 resulting from the ORR can block the smallest pores within the electrode, rendering much of the electrode unusable for the electrochemical reactions. These studies clearly show that both the peroxide growth and electrode microstructure must be considered in unison in order to address the challenge of improving Li-air battery performance.

Computational simulation can be a valuable tool in assessing the effects of the electrode microstructure and peroxide growth on the Li-air battery performance. Only a few numerical models have been reported for the non-aqueous Li-air battery so far.[4,21,36–39] Most of the studies are based on 1D, transient, isothermal models of non-aqueous Li-air systems with carbonate-based electrolytes and assume Li_2O_2 to be the primary discharge product. Sandu et al.[38] modeled the growth of the discharge products as a change in average pore size and showed that O_2 diffusion is limited within the electrolyte. They were able to study the effects of current density, electrode thickness, and O_2 partial pressure on the specific capacity. Andrei et al.[36] developed a model to predict the spatial distribution of the pore volume within the Li-air cell and found that pore blocking exists at the end of discharge. They also explored the beneficial effects of incorporating non-uniform catalyst distribution within the electrolyte and proposed the use of partially-wetted electrodes to reduce the O_2 diffusion length. Xue et al.[30] considered the pore size distribution in their model in order to predict the loss of cell performance attributed to three factors: loss of reaction area, pore blocking, and electrical insulation. Albertus et al.[21] developed a model to consider Li_2CO_3 as the primary discharge product. Li and Faghri[4] developed a 2D non-isothermal model and studied the effects of cathode structures with non-uniform porosity distributions. Wang[40] extended the analysis of the effects of ice formation in PEM fuel cells to Li_2O_2 formation in Li-air batteries and showed that the Li_2O_2 growth mode (via different simplified electrode morphologies) could have significant effects on the performance of the Li-air cell. Wang and Cho[41] developed an approximate analytical model to correlate the cell performance with bulk geometric parameters such as porosity, tortuosity, and the Damköhler number. Sahapatsombut et al.[37] modeled the cell charging performance in addition to discharge. Finally, Sahapatsombut et al.[39] modeled electrolyte degradation effects by considering the growth of Li_2O_2 and Li_2CO_3 in unison. Their model was able to capture the decreasing capacity retention that occurs during repeated cycling of the Li-air cell (about 5% capacity retention per cycle after 10 cycles).

The above mentioned models can all be described as *macroscopic* models since they rely on using volume-averaged structures and effective parameters of the electrode to develop results. In such models, the porous three-phase electrode/electrolyte/peroxide matrix within the cathode is represented as a single continuum, where the electrode structure is characterized using bulk geometric parameters such as porosity, surface area, and tortuosity. Additionally, a necessary assumption is that the electrode microstructure is composed entirely of simple geometric shapes (such as flat plates, cylinders, and spheres) in order to develop the analytical correlations for the electrode's bulk geometric parameters. In these works, the growth of Li_2O_2 can only be captured as a change in bulk porosity throughout the cell, expressed as a function of the ORR rate. As a result, macroscopic models lack the capabilities to predict the effects of the precise electrode and peroxide microstructures that are found in real Li-air systems.

In this work, a pore-scale (or microscale) transport resolved model of the non-aqueous Li-air battery is developed that accounts for the species/charge transport and reaction kinetics across the separate phases of electrolyte, electrode, and peroxide in the porous cathode. Unlike macroscopic models[4,21,36–39,42] that rely on the use of simplified electrode structures, this pore-scale model can take any structure of the electrode and peroxide as a geometric input, making it possible to study the effects that the detailed electrode microstructure and Li_2O_2 growth buildup have on the system-level performance of the Li-air battery. This approach will contribute to the understanding of the electrode morphological effects, which can aid in the design of better electrodes. Similar microscale models have provided unprecedented insight into the transport phenomena in lithium ion batteries[43–48] and vanadium flow batteries.[49,50] Although a pore-scale approach is computationally intensive, the aid of widely available parallel computing facilities will make this microscale model a feasible and powerful tool in understanding the physics that corresponds more closely to the physical Li-air battery.

This paper is organized as follows. Model development section describes the theoretical and numerical background of this microscale model, including the assumptions, governing equations, parameters and a discussion of the Li_2O_2 growth model with a thickness-dependent Li_2O_2 conductivity used in this study. Results and discussion section details the simulation results, including experimental validation and test cases that analyze the effects of various operating parameters and electrode microstructures. Concluding remarks and recommendations for further study are given in Conclusion section.

Model Development

The ion/charge transport and the electrochemistry of a non-aqueous Li-air battery is modeled by solving the coupled, nonlinear differential equations that describe the species and charge balance within the cell. Once the proper parameters, initial/boundary conditions and phase geometries are defined, the governing equations are discretized and solved using an in-house parallel simulation program.

The details of the microscale model are presented as follows. The primary assumptions of the present study are outlined in Assumptions section. The notations used herein to describe the domain regions and phase boundaries are defined in Domain subregions section. The governing equations that describe the species and charge transport are given in Governing equations section. Reaction rate expression section includes the details about modeling the electrochemical reactions that take place at the electrode surface via the Butler-Volmer equation. Boundary and initial conditions used in this study are described in Boundary and initial conditions section. Li_2O_2 growth model and thickness-dependent conductivity section summarizes the growth mechanism and thickness-dependent conductivity model to account for the Li_2O_2 formation during discharge. Finally, details of the numerical implementation are provided in Numerical implementation section.

Assumptions.— Unless otherwise stated, the following assumptions are observed for all cases in the model:

- The electrolyte phase in the model is assumed to be binary monovalent and defined with the properties of 1,2-Dimethoxyethane (DME).[8]
- Li_2O_2 is the primary discharge product; side reactions are not considered.
- Li_2O_2 is non-dissolving and its electrical conductivity is thickness-dependent.
- The ORR occurs at the junction between electrolyte and electrode or Li_2O_2.[12,18,51]
- Reaction kinetics are the same for both the electrode and Li_2O_2 surface.[21,37,52]

- All pores within the porous cathode matrix are completely submerged in electrolyte.
- The overpotential of the anode reaction is negligible.[53]
- Transport of Li^+ and O_2 through the Li_2O_2 layer are negligible.[54,55]
- There is a constant supply of Li^+ and O_2 from the surroundings.
- Growth of Li_2O_2 is reaction limited.
- O_2 is assumed to be the only gaseous species dissolved in the electrolyte.
- Degradation of electrolyte and electrode are not considered.
- Convective mass fluxes in the electrolyte are negligible.
- The system is in isothermal conditions.

Domain subregions.— As shown in Fig. 1, the two-dimensional computational domain extends from the left hand side which represents the lithium metal boundary at $x = 0$ to the right hand side which represents the current collector and environmental oxygen boundary conditions at $x = L_x$. The computational domain is also periodic in the y-direction with the lower boundary at $y = 0$ and upper boundary at $y = L_y$. The microscale model accounts for the species and/or charge transport across the three distinct phases of liquid electrolyte, solid carbon electrode, and solid lithium peroxide, denoted by Ω_1, Ω_2, and Ω_3, respectively. The entire simulation domain Ω consists exclusively of these three non-overlapping subdomains, with $\Omega = \Omega_1 \cup \Omega_2 \cup \Omega_3$. The interfaces between two subregions are denoted by Γ_{jk} where $\Gamma_{jk} = \Omega_j \cap \Omega_k$. For example Γ_{12} represents all boundaries between the liquid electrolyte Ω_1 and solid electrode Ω_2. An illustration of the subregions is shown in Fig. 1. Herein, references to a 'solid' phase means both electrode and Li_2O_2 phases, i.e. $\Omega_2 \cup \Omega_3$.

Governing equations.— The governing equations describe the transport of species (Species conservation section) and charge (Charge conservation section) as given by the concentrated binary electrolyte theory applied at the continuum level.[56]

Species conservation.—The concentrations of species O_2 and Li^+ are solved in the electrolyte phase of the battery (denoted by subscript 1). The mass conversion of O_2 is given by the diffusion equation:

$$\frac{\partial c_{O_2}}{\partial t} = \nabla \cdot \left(D_{O_2} \nabla c_{O_2}\right) \quad \text{in } \Omega_1 \qquad [2]$$

where c is the concentration, D the diffusion coefficient, and the subscript represents species (O_2 is given here in Eq. 2). The conservation of Li^+ is governed by diffusion with an additional term to account for the mass flux due to an electrolytic current[56] as follows

$$\frac{\partial c_{Li^+}}{\partial t} = \nabla \cdot \left(D_{Li^+} \nabla c_{Li^+} - \frac{t_+}{F}\mathbf{i}\right) \quad \text{in } \Omega_1 \qquad [3]$$

where t_+ is the transference number, F is the Faraday constant (96,485 C mol^{-1}), and $\mathbf{i}$ is the electrolytic current, given by:

$$\mathbf{i} = -\kappa_1 \nabla \varphi_1 - \frac{2RT\kappa_1}{F}(t_+ - 1)\left(1 + \frac{\partial \ln f}{\partial \ln c_{Li^+}}\right)\nabla \ln c_{Li^+} \quad \text{in } \Omega_1 \qquad [4]$$

where φ_1 is the electric potential in the electrolyte phase, κ_1 is the electrolytic conductivity, R is the universal gas constant (8.3143 J mol^{-1} K^{-1}), T is the absolute temperature, and f is the activity coefficient. The term $\partial \ln f / \partial \ln c_{Li^+}$ is approximated to be zero.[36]

Charge conservation.—The electrostatic potential within the battery is solved using the conservation of charge in all relevant phases of the battery. The charge transport process in the Li_2O_2 is very complicated, most likely involving electron tunneling effects,[22] semi-metallic surface conductivity,[8,18,20,57] polaron migration,[19,58] or some combination thereof.[59] For this work, we assume that Ohm's law describes the conservation of charge in the electrode and solid Li_2O_2 phases (denoted by subscript 2 and 3, respectively):

$$0 = \nabla \cdot (\sigma_2 \nabla \varphi_2) \quad \text{in } \Omega_2 \qquad [5]$$

$$0 = \nabla \cdot (\sigma_3 \nabla \varphi_3) \quad \text{in } \Omega_3 \qquad [6]$$

where φ_2 and φ_3 are, respectively, the electrode and Li_2O_2 phase potentials and σ_2 and σ_3 are, respectively, the electrical conductivities of the electrode phase and the Li_2O_2 phase. The conductivity of the Li_2O_2 phase is dependent on its thickness and will be addressed in later sections. In the electrolyte, a modified version of Ohm's law known as the drift-diffusion equation is used to model the electrostatic potential:[36]

$$0 = \nabla \cdot \left[\kappa_1 \nabla \varphi_1 + \frac{2RT\kappa_1}{F}(t_+ - 1)\left(1 + \frac{\partial \ln f}{\partial \ln c_{Li^+}}\right)\nabla \ln c_{Li^+}\right] \quad \text{in } \Omega_1 \qquad [7]$$

The cell voltage can be calculated by taking the difference between the electrode-phase voltage at the current collector boundary with the electrolyte-phase voltage at the lithium metal boundary, i.e., $U = \varphi_2|_{x=L_x} - \varphi_1|_{x=0}$. The discharge process is considered complete when the cell voltage drops below a cutoff voltage of 2.0 V.[8]

Reaction rate expression.— The ORR takes place on the electrode/Li_2O_2 surface and accounts for the electrochemically-induced fluxes of species and charge as well as the formation of Li_2O_2. A one-step reaction process is assumed for this study following Eq. 1 that takes place on the electrolyte/solid interface, i.e., $\Gamma_{12} \cup \Gamma_{13}$. As shown in Fig. 1, it is assumed that new Li_2O_2 will form over existing buildup, as deduced from experimental observations where electrode catalysts lose their effectiveness after a layer of Li_2O_2 has formed above the cathode surface.[12,18,51] The current flux, denoted by $\mathbf{i} \cdot \hat{\mathbf{n}}$, is calculated using the Butler-Volmer equation[36,52]

$$\mathbf{i} \cdot \hat{\mathbf{n}} = 2Fk_c\left(\frac{c_{O_2}}{c_{O_2,\text{ref}}}\right)\left(\exp\left[\frac{(1-\beta)F}{RT}\eta\right] - \exp\left[\frac{-\beta F}{RT}\eta\right]\right) \quad \text{on } \Gamma_{12} \cup \Gamma_{13} \qquad [8]$$

where the molar concentrations are taken at the surface of the liquid/solid interface, $\hat{\mathbf{n}}$ denotes the unit normal pointing outward from the solid surface, k_c is the reaction rate coefficient, β is the symmetry factor, and η is the surface overpotential given by

$$\eta = \varphi_{2\cup 3} - \varphi_1 - U_0 \text{ on } \Gamma_{12} \cup \Gamma_{13} \qquad [9]$$

where $\varphi_{2\cup 3}$ represents the electrostatic potential in either the electrode or Li_2O_2 taken at the active surface, φ_1 is the electrostatic potential in the liquid phase by the active surface, and U_0 is the thermodynamic voltage for the overall reaction in Eq. 1. The corresponding mole flux for species $i \in \{O_2, Li^+, Li_2O_2\}$ denoted by $\mathbf{N}_i$ from the electrochemical reactions can be calculated from the current flux using Faraday's Law:

$$\mathbf{N}_i = \frac{s_i}{nF}\mathbf{i} \qquad \text{on } \Gamma_{12} \cup \Gamma_{13} \qquad [10]$$

where s_i is the stoichiometric coefficient of the reaction for species i as per Eq. 1, n is the number of electrons transferred in the reaction, and $n = 2$ for Eq. 1.

It should be reiterated that the microscale model considers the ORR given by the Butler-Volmer equation (Eq. 8) as a surface flux boundary condition between all liquid/solid interfaces, i.e. $\Gamma_{12} \cup \Gamma_{13}$, while macroscale models incorporate the ORR as a volumetric source term within a homogenous electrode/electrolyte volume. The surface quantities of concentration and voltage at the solid/electrolyte interface dictate the conditions for the ORR, so attaining these values next to the active surface is important for accurately modeling the microscale electrochemical behavior of the Li-air battery. In macroscale models, only bulk values (meaning volume-averaged values that do not reflect the quantities found next to the interface) for concentration and voltage are used since the porous electrolyte/electrode matrix is treated as a single continuum,[21,36,60] although localized values can be

Table I. Boundary conditions used in the simulation. Periodic boundary conditions are used for all variables at the $y = 0$ and $y = L_y$ boundaries.

Sub-region	Variable	$x = 0$	$x = L$	$\Gamma_{12} \cup \Gamma_{13}$	Γ_{13}
Ω_1	c_{O_2}	$\frac{\partial c_{O_2}}{\partial x} = 0$	$c_{O_2} = c_{O_2}^{ext}$	$\frac{\partial c_{O_2}}{\partial x} = \mathbf{N}_{O_2} \cdot \hat{\mathbf{n}}$	---
Ω_1	c_{Li^+}	$c_{Li^+} = c_{Li^+}^{ext}$	$\frac{\partial c_{Li^+}}{\partial x} = 0$	$\frac{\partial c_{Li^+}}{\partial x} = \mathbf{N}_{Li^+} \cdot \hat{\mathbf{n}}$	---
Ω_1	$c_{Li_2O_2}$	$\frac{\partial c_{Li_2O_2}}{\partial x} = 0$	$\frac{\partial c_{Li_2O_2}}{\partial x} = 0$	$\frac{\partial c_{Li_2O_2}}{\partial x} = -\mathbf{N}_{Li_2O_2} \cdot \hat{\mathbf{n}}$	---
Ω_1	φ_1	$\varphi_1 = 0$	$\frac{\partial \varphi_1}{\partial x} = 0$	$\kappa_1 \frac{\partial \varphi_1}{\partial x} = \mathbf{i} \cdot \hat{\mathbf{n}}$	---
Ω_2	φ_2	$\frac{\partial \varphi_2}{\partial x} = 0$	$\sigma_2 \frac{\partial \varphi_2}{\partial x} = I^{ext}$	$\sigma_2 \frac{\partial \varphi_2}{\partial x} = -\mathbf{i} \cdot \hat{\mathbf{n}}$	$\sigma_2 . \frac{\partial \varphi}{\partial x}\vert_2 = \sigma_3 . \frac{\partial \varphi}{\partial x}\vert_3$
Ω_3	φ_3	$\frac{\partial \varphi_3}{\partial x} = 0$	$\frac{\partial \varphi_3}{\partial x} = 0$	$\sigma_3 \frac{\partial \varphi_3}{\partial x} = -\mathbf{i} \cdot \hat{\mathbf{n}}$	$\sigma_2 . \frac{\partial \varphi}{\partial x}\vert_2 = \sigma_3 . \frac{\partial \varphi}{\partial x}\vert_3$

approximated using bulk diffusion models such as Fick's law.[37] In the present study, localized values of concentration and voltage near the active surface are available intrinsically since the liquid and solid phases are distinctively modeled, so no approximations regarding the surface quantities are necessary.

Boundary and initial conditions.— The boundary conditions used to solve for the species and charge transport are summarized in Table I. At $x = L_x$, an external current density (i_{ext}) is applied to the electrode phase, while a Dirichlet oxygen concentration boundary condition equivalent to the solubility of O_2 is applied to the electrolyte ($c_{O_2}^{max}$). At the left end of the electrolyte domain, the lithium metal boundary, the solubility value of Li^+ is applied as a Dirichlet concentration boundary condition ($c_{Li^+}^{max}$),[36] and a reference voltage is applied and assumed constant.[53] Periodic boundary conditions are applied for all variables and phases at the $y = 0$ and $y = L_y$ boundaries. Continuous voltage flux boundary conditions are used at the electrode/Li_2O_2 interface (Γ_{23}). The Butler-Volmer flux (Eq. 8) is applied as a surface flux boundary condition between all electrolyte/solid interfaces, i.e. $\Gamma_{12} \cup \Gamma_{13}$. It should be mentioned that as Li_2O_2 forms, the liquid electrolyte will be displaced out of the porous cathode.[21] As such, this model considers the conservation of electrolyte mass by displacing electrolyte voxels to the left side of our domain whenever a Li_2O_2 voxel forms. The initial concentrations of O_2 and Li^+ ($c_{O_2}^0$ and $c_{Li^+}^0$ respectively) are specified to their respective solubility values c_i^{max} uniformly throughout the electrolyte phase.

Li_2O_2 growth model and thickness-dependent conductivity.— During the ORR, Li_2O_2 forms within the porous cathode, depositing as a solid product on the electrode surface. The morphology and size of Li_2O_2 formation observed in experiments range from micro-sized toroids[9,61,62] to nanoparticles[54,63] and thin rough films,[8,22] depending upon the choice of electrolyte,[16,24,27,63–67] discharge current,[8,62] and catalyst.[8,68] However, previous macroscopic simulations are only able to model the Li_2O_2 growth as a change in bulk porosity within the cell.[21,36–39,69] The electrically insulating effect of the Li_2O_2 is then accounted for as an additional porosity-dependent surface resistance in the overpotential expression.[21] As such, these models are not able to explore the importance of detailed Li_2O_2 morphology on the cell-level performance.[31]

Unfortunately, there is no consensus regarding the specific growth mechanism for the Li_2O_2 discharge product. Viswanathan et al. suggested that electrical insulation limits the growth of Li_2O_2 films to 10 nm[22], although high-capacity experiments (1000 - 10000 $mAhg^{-1}$[6,8–10,51,70]) revealed that the deposition products can grow up to 1 μm in size.[9,61,62] Based on XRD studies,[12] Lu et al.[59] observed a quasi-unifying growth mechanism in which seed layers of Li_2O_2 form up to 10 nm thick sheets, implying charge transport via electron tunneling.[22] The Li_2O_2 thin sheets then grow laterally via semi-metallic surface conduction,[8,18,20,57] and finally stack together to form the observed 1 μm-sized toroids.

In this work, the pore-scale growth of Li_2O_2 is assumed to be kinetic-limited, where the electrolyte phase next to an electrode/Li_2O_2 phase is converted to a solid Li_2O_2 phase if the local peroxide concentration, $c_{Li_2O_2}$, resulting from the ORR exceeds the value for the entire voxel to be occupied by Li_2O_2, following

$$\delta\Omega_1 = \begin{cases} \delta\Omega_1, c_{Li_2O_2} < \rho_{Li_2O_2}/M_{Li_2O_2} \\ \delta\Omega_3, c_{Li_2O_2} \geq \rho_{Li_2O_2}/M_{Li_2O_2} \end{cases} \quad \text{in } \Omega_1 \qquad [11]$$

where $\delta\Omega_1$ is a single voxel element of the electrolyte phase and $\delta\Omega_3$ is a single voxel element of the Li_2O_2 phase, and $\rho_{Li_2O_2}$ and $M_{Li_2O_2}$ are the density and molecular weight of Li_2O_2, respectively. Using this mass conserving growth mechanism of Li_2O_2, the distinct phase boundaries can be tracked and visualized "in situ" during the ORR so as to provide keen insight into the impact of the peroxide microstructure on cell performance.

The conductivity of Li_2O_2 has been generally reported in the range of 10^{-9}-10^{-13} S/cm.[55,59,71] However, Tian et al.[72] reported a conductivity of 2×10^{-7} S/cm for the amorphous Li_2O_2 and a conductivity of 2×10^{-16} S/cm for the crystalline Li_2O_2. Viswanathan et al. conducted density functional theory (DFT) simulations and showed that the conductivity of Li_2O_2 thin films decreases with increasing Li_2O_2 thickness.[22] Figure 2a shows the Li_2O_2 conductivity, σ, versus thickness, δ, plot based on the DFT results of Viswanathan et al.,[22] where the correlation between σ and δ is fitted using a power law as

$$\sigma_3(\delta) = 10^7 \delta^{-17.18} \left[\mathrm{S/m}\right] \qquad [12]$$

Equation 12 gives a continuous decrease in conductivity with Li_2O_2 film thickness. However, when $\sigma_3 \leq 10^{-12}$ S/m, the large voltage gradients across the Li_2O_2 phase cause numerical instabilities and hence, in present simulations, the Li_2O_2 is assumed to be insulating when the Li_2O_2 conductivity is smaller than 10^{-12} S/m. The corresponding critical insulation thickness, δ_{crit}, of the Li_2O_2 is 12.6 nm, i.e., the electrode is considered electrically insulated when the Li_2O_2 layer reaches 12.6 nm thick.

Figure 2b shows the comparison of discharge profiles between the present thickness-dependent Li_2O_2 conductivity model, Eq. 12, and constant Li_2O_2 conductivities of 10^{-10} and 10^{-11} S/m, respectively, for a bare fin cathode (a planar electrode without nanostructure features) with local current density of 2.5 mA m_c^{-2}. The results show that the discharge capacity is very sensitive to the conductivity of Li_2O_2. For both cases of $\sigma_3 = 10^{-11}$S/m and the thickness-dependent conductivity, the discharge process is complete when the Li_2O_2 layer growing on the electrode surface becomes electrically insulated. A higher Li_2O_2 conductivity leads to a larger discharge capacity as a result of a thicker Li_2O_2 buildup. The step-like discharge profiles shown in these cases are due to the fact that in our simulation Li_2O_2 grows in distinct layers causing non-continuous drops in the cell voltage. As shown in Fig. 2b, for the case of $\sigma_3 = 10^{-10}$S/m, Li_2O_2 continues to grow until the cell voltage drops below the discharge cutoff voltage of 2.0 V.

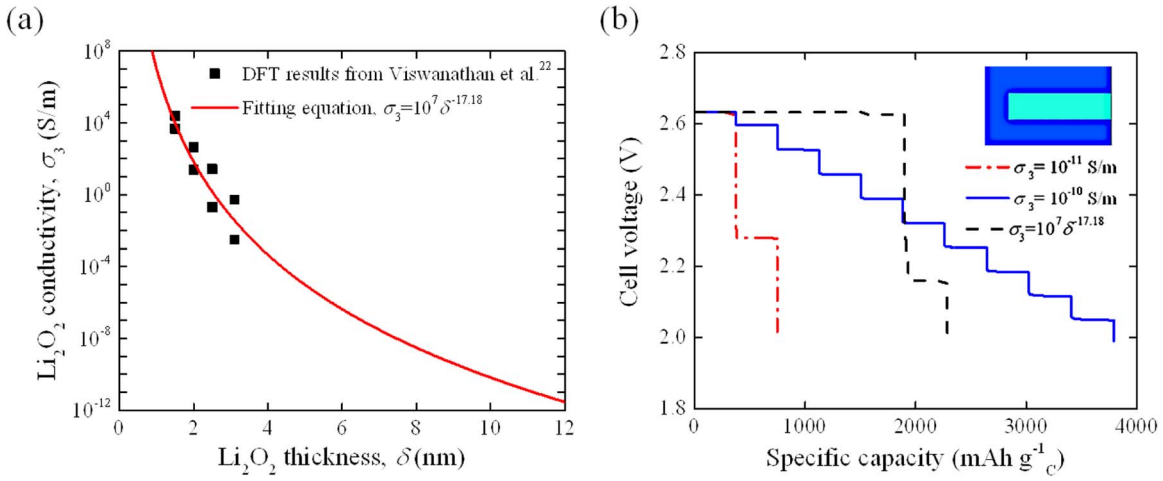

Fig. 2. (a) Conductivity of Li_2O_2 as a function of Li_2O_2 thickness. The symbols represent the results from Viswanathan et al.[22] based on DFT calculations and the solid line is a power law fitting. (b) Comparison of discharge profile between thickness-dependent conductivity and constant conductivities for a bare fin cathode at the local current density of 2.5 mA m_c^{-2}.

It is important to note that, once the electrode is insulated by the Li_2O_2 buildup, electrons can no longer penetrate through the Li_2O_2 layer to participate in the ORR for continued Li_2O_2 growth. The discharge process stops when either the electrode is insulated or cell voltage drops below the cutoff voltage of 2.0 V. The specific discharge capacity can be calculated as $Q = \int_0^{t_f} \iint_{A_s(t)} i_{local} dA_s dt$, where t_f is the total discharge time, and i_{local} and A_s can be functions of both space and time under galvanostatic discharge conditions due to complex electrode structures and possible pore blocking events. Assuming uniform local current density and constant specific area during discharge (i.e., i_{local} and A_s are both constant), the specific discharge capacity is simplified as $Q = i_{local} A_s t_f$, where t_f is related to the total amount of Li_2O_2 deposited on the cathode surface $m_{Li_2O_2}$ following $t_f = m_{Li_2O_2}/(M_{Li_2O_2} N_{Li_2O_2} A_s m_c)$. Here, $M_{Li_2O_2}$ is the molar mass of Li_2O_2, and m_c is the mass of the electrode. Based on Eq. 10, the mole flux of Li_2O_2 perpendicular to the electrode surface follows $N_{Li_2O_2} = \frac{s_{Li_2O_2}}{n} \frac{i_{local}}{F}$. The specific discharge capacity as a function the total amount of Li_2O_2 formation can hence be written as

$$Q = \frac{nF}{s_{Li_2O_2} M_{Li_2O_2}} \frac{m_{Li_2O_2}}{m_c} \quad [13]$$

Based on the self-limiting nature of the Li_2O_2 growth, the insulation limit of the specific discharge capacity, Q_{ins}, can be determined by calculating $m_{Li_2O_2}$ in Eq. 13 using the critical insulation thickness δ_{crit}. Assuming a uniform local current density and a constant active surface area during discharge, the total amount of Li_2O_2 deposited in the insulation limit is $m_{Li_2O_2} = \rho_{Li_2O_2} A_s \delta_{crit} m_c$. Equation 13 can hence be rewritten based on the critical insulation thickness δ_{crit} as

$$Q_{ins} = \frac{nF\left(A_s \rho_{Li_2O_2} \delta_{crit}\right)}{s_{Li_2O_2} M_{Li_2O_2}} \quad [14]$$

Equation 14 predicts the insulation limit of the specific discharge capacity for an electrode of constant specific area during discharge. For the case where pore blocking occurs, the electrode surface area is changed locally, which violates the constant specific area assumption. The active surface area decreases as a result of pore blocking, which leads to capacity fading.

Numerical implementation.— The simulation program is written in-house using FORTRAN 90 and the Message Passing Interface (MPI) for parallel processing via 1D domain decomposition. An implicit 2D finite-volume method (FVM)[73] is used to linearize and solve for the coupled, nonlinear governing transport equations. As for the mesh, on one hand, a fine mesh is preferred to guarantee the growth and the thickness-dependent conductivity of Li_2O_2, as well as the electrode microstructure, are modeled with high accuracy. On the other hand, the grid size should be large enough to avoid the breakdown of the continuum assumption. Therefore, a uniform Cartesian mesh with a grid resolution of 2 nm, well above the calculated Debye length of 0.3 nm, is used to model the nanoscale Li_2O_2 formations with adequate fidelity. A tolerance of 1×10^{-10} is imposed for the relative residual error for the voltage and concentration fields. Additionally, a tolerance of 1×10^{-4} is imposed to ensure the overall conservation of charge is maintained (calculated based on the relative difference between the total current drawn at the current collector and the total current drawn across the surface of the electrolyte/solid interface). Simulations were performed using 4 nodes of the Stampede cluster with Intel Xeon Phi Co-processors at the Texas Advanced Computing Center.

Results and Discussion

The results are organized as follows. Model validation section contains the model validation against the experimental work of Lu et al.[8] Effect of operating parameters section shows the effects of applied current density and ORR rate coefficient on cell performance. Effect of electrode structure section investigates the effects of electrode structures on Li_2O_2 growth and discharge profile. All simulations are performed under galvanostatic discharge conditions. All reported current densities and capacities are normalized to the surface area and mass, respectively, of the carbon electrode prior to discharge (denoted by subscript "c"). The parameters listed in Table II are used in all cases unless otherwise stated.

Model validation.— The pore-scale model is validated against the experimental work of Lu et al.[8] The parameters used in Lu et al., including an ether-based electrolyte (0.1M $LiClO_4$ DME) as listed in Table II, are applied in the simulation. A nanostructured electrode was constructed to match the 85% porosity and 100 $m^2\ g_c^{-1}$ specific area,[8] and the spacing of the nanostructure was chosen to be 30 nm to match the minimum pore size in Lu et al.[8] Figure 3 shows the comparison of discharge profile between the present pore-scale model and Lu et al.'s experiments at local current density of 2.5 mA m_c^{-2}. As shown in Fig. 3, the present pore-scale model agrees well with the experiments, with an average relative error of only 2.24% in voltage. The specific discharge capacity of the cell from the pore scale model is 2813 mAh g_c^{-1}, which is only 4.76% larger than the experimental value of 2685 mAh g_c^{-1}. The largely constant voltage during the discharge process can be explained by the relatively high conductivity ($>10^{-8}$ S/m) of

Table II. Simulation parameters.

Parameter	Value	Unit	Symbol	Ref.
Cell & Electrode Properties				
Unit cell width	0.64	μm	L_x	---
Unit cell height	0.58	μm	L_y	---
Initial Porosity	0.85	---		8
Electrode Specific Area	100	$m^2\ g_c^{-1}$	A_s	8
Species Transport Properties				
O_2 diffusion coefficient	4.0×10^{-9}	$m^2\ s^{-1}$	D_{O_2}	8
Li^+ diffusion coefficient	1.33×10^{-9}	$m^2\ s^{-1}$	D_{Li^+}	8
Oxygen solubility	8.76	$mol\ m^{-3}$	$c_{O_2}^{max}$	8
Lithium-ion solubility	100	$mol\ m^{-3}$	$c_{O_2}^{max}$	8
Li_2O_2 solubility	46643	$mol\ m^{-3}$	$c_{Li_2O_2}^{max}$	Calculated
Charge Transport Properties				
Electrolyte conductivity	0.552	$S\ m^{-1}$	κ_1	41
Electrode conductivity	212	$S\ m^{-1}$	σ_2	8
Transference number of Li	0.5	---	t_+	8
Activity coefficient variation	0	---	$\partial \ln f / \partial c_{Li^+}$	36
Local current density	2.5	$mA\ m_c^{-2}$	i_{local}	8
Kinetic Properties				
ORR rate coefficient	3.63×10^{-9}	$mol\ m^{-2}s^{-1}$	k_c	Estimated
Symmetry factor	0.5	---	β	37
Electrons transferred in overall reaction	2	---	n	---
General Properties				
Molecular weight of peroxide	45.88	$g\ mol^{-1}$	$M_{Li_2O_2}$	---
Mass Density of Vulcan carbon	2.56×10^5	$g\ m^{-3}$	ρ_c	60
Mass Density of Li_2O_2	2.14×10^6	$g\ m^{-3}$	$\rho_{Li_2O_2}$	36
Operating Temperature	300	K	T	---
Thermodynamic voltage	2.96	V	U_0	28

the Li_2O_2 layer of thickness up to 8 nm (i.e., 4 discrete layers of 2 nm each). As some area of the Li_2O_2 layer reaches 10 nm thick (i.e., 5 discrete layers of 2 nm each), the cell voltage starts to drop more obviously, until a large voltage drop occurs with 10 nm Li_2O_2 buildup on the entire electrode surface. This is followed by another large voltage drop below its cutoff value causing the discharge process to stop. The inset of Fig. 3 shows a 0.1 μm × 0.1 μm snapshot of the nanostructured cathode with Li_2O_2 deposition (in yellow) when the cell voltage falls below the cutoff voltage of 2.0 V and no pore blocking is observed.

Note that, for the electrode microstructure considered (H = 10 nm, S = 30 nm), Eq. 14 predicts the insulation limit of the specific discharge capacity of 3150 mAh g_c^{-1}, which is higher than both the simulated (2813 $mAhg_c^{-1}$) and experimentally determined (2685 mAh g_c^{-1}) values. This is because the Li_2O_2 buildup does not globally reach its critical insulation thickness when the discharge process stops at the discharge cutoff voltage of 2.0 V.

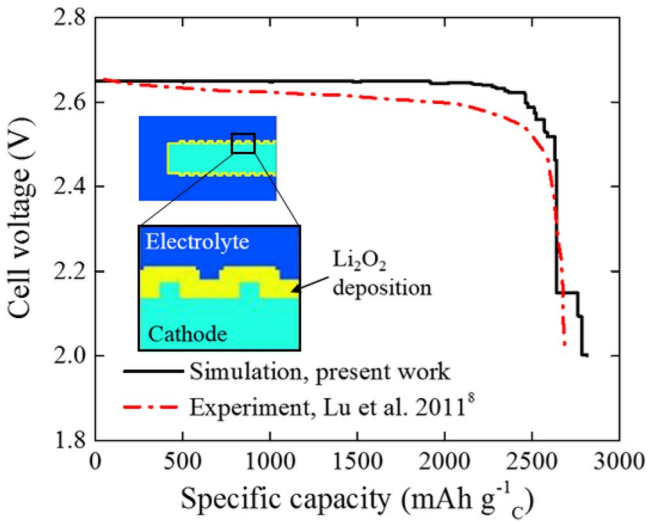

Fig. 3. Model validation against experiment of Lu et al.[8] at the current density of 2.5 mA m_c^{-2} for a nanostructured electrode of 85% porosity and 100 $m^2\ g_c^{-1}$ specific area.[8] The inset shows the zoomed-in snapshot of Li_2O_2 formation on the electrode surface when the cell voltage reaches the cutoff voltage of 2.0 V.

Effect of operating parameters.— In this section, the effects of different discharge current density and ORR rate coefficients on the discharge capacity and discharge voltage are explored. The nanostructured electrode with spacing of 30 nm, height of 10 nm, 85% porosity, and 100 $m^2\ g_c^{-1}$ specific area (i.e. the validation case) is used for all simulations in this section. As mentioned in Model validation section, no pore blocking occurs for this nanostructured cathode at $i_{local} = 0.5$ mA m_c^{-2} and $k_c = 3.63 \times 10^{-9}$ mol $m^{-2}s^{-1}$.

Effect of local current density.—The local current density affects the growth rate of Li_2O_2 and is thus an important parameter to examine. Figure 4a shows the cell voltage versus the specific capacity for the local current densities of 0.5, 1.0, 2.5, and 20 mA m_c^{-2}, respectively when keeping $k_c = 3.63 \times 10^{-9}$ mol $m^{-2}s^{-1}$. The results show that the discharge cell voltage decreases with applied current density from 2.731 V at 0.5 mA m_c^{-2} to 2.541 V at 20 mA m_c^{-2}, due to a larger overpotential (and larger reaction losses) as a result of an increased current. The specific discharge capacity also decreases with local current density, from 3038 mAh g_c^{-1} at 0.5 mA m_c^{-2} to 2536 mAh g_c^{-1} at 20 mA m_c^{-2}. This is because a smaller local current density corresponds to a higher cell voltage, which allows for a longer discharge time before it reaches the cutoff voltage of 2.0 V. As the local current density decreases to 0.5 mA m_c^{-2}, the specfic capacity finally reaches its insulation limit of 3150 mAh g_c^{-1}, predicted by Eq. 14. As shown in the inset of Fig. 4a, the zoomed-in snapshots of Li_2O_2 deposited on the electrode surface at the end of discharge demonstrate

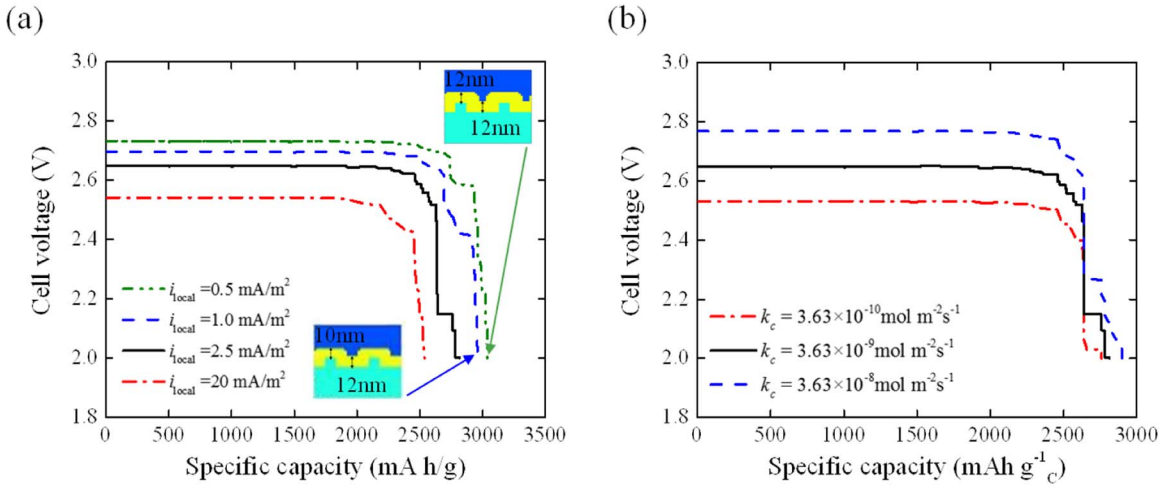

Fig. 4. Discharge cell voltage as a function of specific capacity (a) at different local current densities and (b) at different ORR rate constants. The inset in (a) shows the zoomed-in (0.1 μm × 0.1 μm) snapshots of Li_2O_2 morphology on the electrode surface where a uniform Li_2O_2 layer of 12 nm thick is formed for the local current density of 0.5 mA m_c^{-2} as compared to a non-uniform Li_2O_2 layer for the case of 1 mA m_c^{-2}. All simulations are performed with a nanostructured cathode with spacing $S = 30$ nm, height $H = 10$ nm, and 85% porosity. The domain is a 0.64 μm × 0.58 μm periodic unit cell. Other baseline operating conditions are listed in Table II.

the reach of critical insulation thickness of 12 nm (the next thickness increment is 14 nm, exceeding δ_{crit} of 12.6 nm) for the entire electrode at i_{local} =0.5 mA m_c^{-2}, compared to only locally reaching the critical Li_2O_2 thickness for i_{local} =1 mA m_c^{-2}.

Effect of ORR rate coefficient.—In experiments where various catalysts were applied to the electrode surface, improvements in discharge voltage were observed during the initial phases of discharge before the Li_2O_2 layer was thick enough to envelop the catalysts on the cathode surface.[12,18,51] The catalyst influences the discharge cell voltage by affecting the ORR rate coefficient, k_c, which dictates the efficiency to which the ORR is carried out on the cathode surface. Figure 4b shows the comparison of discharge curves from present pore-scale simulations using ORR rate coefficients of $k_c = 3.63 \times 10^{-10}$, 3.63×10^{-9}, and 3.63×10^{-8}mol $m^{-2}s^{-1}$. The results show that the discharge specific capacity does not change significantly with the ORR rate coefficient k_c, because k_c only affects the speed of the reaction, not the quantity of reactions occurring. On the other hand, a higher k_c improves the cell voltage, a trend that is echoed in previous macroscope models.[36,37] For kinetic-limited growth of Li_2O_2 during galvanostatic discharge, the improvement in cell voltage with increasing ORR rate coefficient is due to the reduction in reaction losses and a lower overpotential η governed by the Butler-Volmer relation (Eq. 8). However, in real battery practice, the increase of cell voltage by the use of catalysts may not sustain through the entire discharge process due to the coverage of the porous electrode surface by Li_2O_2.

Effect of electrode structure.— In addition to the aforementioned parameters, the electrode structure also has a strong effect on the discharge capabilities of the non-aqueous Li-air battery. As discussed in the introduction, Tran et al.[35] showed that the pore size of the hierarchal structure of the electrode material plays a key role in determining the cell capacity.[35] Previous macroscopic models can only observe the effects of bulk geometric parameters, such as porosity, surface area, and tortuosity in volume-averaged domains that assume a homogenous distribution of simplified electrode structures such as cylinders, spheres, and plates.[4,21,36–42,69] Pore-scale simulations are conducted here to examine the effects of nanostructure spacing and height of an electrode of around 85% porosity and 100 m^2 g_c^{-1}specific area at galvanostatic conditions with a local current density of 2.5 mA m_c^{-2}. As shown in Fig. 5a, electrodes with square nanostructures of height H, width W, and spacing H are examined in a periodic unit cell with dimensions of 0.64 μm × 0.58 μm, where the periodic boundary conditions are utilized at the top and bottom boundaries of the domain.

Effect of structure spacing.—Although nanostructures increase the surface area of the electrode, they can also cause pore blocking due to Li_2O_2 buildup during the discharge process, thus rendering the additional surface area unutilized for the ORR. As the square nanostructured electrode shown in Fig. 5a, the effect of varying nanostructure spacing S is examined while keeping $S + W = 40$ nm the same so that the electrode surface area is constant. The height of the nanostructure, H, is kept at 10 nm for all cases. Figure 5b shows the discharge cell voltage versus the specific capacity under galvanostatic discharge with a local current density of 2.5 mA m_c^{-2} for nanostructure spacings of 4, 16, 30, and 36 nm. The results show that the specific discharge capacity increases monotonically with nanostructure spacing. Note that increasing nanostructure spacing while keeping surface area constant leads to an increase in the electrode specific area and hence an increase in the insulation limit of the specific capacity as predicted by Eq. 14. It is also shown in Fig. 5b that, the discharge voltage does not change significantly with nanostructure spacing.

To quantitatively investigate the effect of nanostructure spacing, Fig. 6a plots the specific discharge capacity (Q) as a function of the nanostructure spacing (S) from pore-scale simulations (symbols) as compared to the insulation limit determined by Eq. 14 (red line) for S = 4, 8, 12, 16, 20, 26, 30, and 36 nm. The results show that the specific discharge capacity increases monotonically from 2164 to 2923 mAh g_c^{-1} when S increases from 4 to 36 nm. For all cases investigated, the simulated specific capacities are lower than the insulation limit, indicating that the Li_2O_2 buildup on the electrode surface does not globally reach its insulation thickness when the discharge processes are terminated due to cell voltage falling below the cutoff voltage of 2.0 V.

As shown in Fig. 6a, the results from the pore-scale simulation reveal two regimes for the effect of nanostructure spacing on specific discharge capacity with two distinct slopes for the Q-S relation: i) a regime with a relative large slope at small nanostructure spacings (i.e., S = 4, 8, 12, 16, 20 nm) and ii) a regime with a relative small slope for large nanostructure spacings (i.e., S = 26, 30, 36 nm), separated by pore blocking events. Two time scales are associated with the Li_2O_2 growth: the time for a nano-pore to be blocked is approximated by $t_b = S/(2d\delta/dt)$ and the time for the electrode to be fully insulated is $t_{ins} = \delta_{crit}/(d\delta/dt)$. For $S > 2\delta_{crit}$, it yields $t_{ins} < t_b$ and the electrode becomes fully insulated before the pores are blocked by Li_2O_2. The regime of $S > 2\delta_{crit}$ hence denotes the non-pore-blocking regime. In the non-pore-blocking regime, the simulation results show smaller specific capacities as compared to the insulation limit predicted by Eq. 14. Because for a nanostructured electrode, the critical insulation

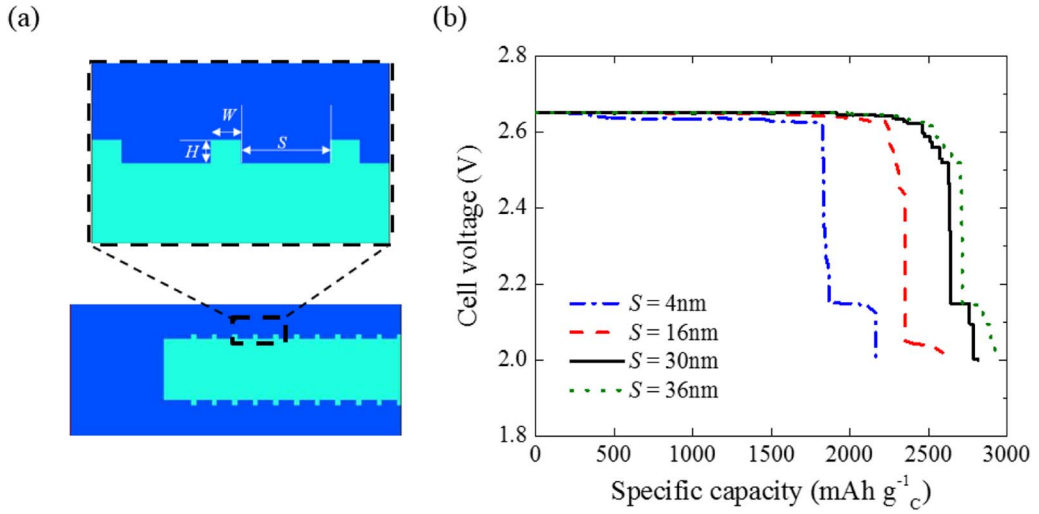

Fig. 5. (a) Schematic of square nanostructured cathode, where W, S and H denote the width, spacing and height of the nanostructure, respectively. (b) Discharge cell voltage as a function of specific capacity at different nanostructure spacings. The domain is a 0.64 μm × 0.58 μm periodic unit cell subject to local galvanostatic discharge at 2.5 mA m_c^{-2}.

thickness of Li_2O_2 is only reached locally due to uneven Li_2O_2 deposition along the electrode surface while parts of the electrode still remain conductive. For these cases, the discharge process is stopped due to the cell voltage failing below 2.0 V. In addition, the simulated slope of the Q-S relation is similar to the slope predicted by Eq. 14 for the insulation limit. This is because for both simulation and simplified model, the nanostructure spacing affects the specific volume and thus the specific area of the cathode. As for the regime of $S < 2\delta_{crit}$, $t_{ins} > t_b$ nano-pores are blocked before the electrode becomes fully insulated, or the so-called pore-blocking regime. In this regime, the simulation results show a larger slope of the Q-S relation than that predicted by Eq. 14 because of the further reduction in specific area (and increase of local current density and overpotential) due to pore blocking during discharge. At the limit of $S = 0$ nm and $S = 40$ nm, we recover the cases for bare fin electrodes. For both cases, the specific capacities are much smaller than those of nanostructured electrodes due to the reduction of surface area.

Figure 6b shows the plateau discharge voltage as a function of nanostructure spacing of S = 4, 8, 12, 16, 20, 26, 30, and 36 nm, where the discharge voltage monotonically increases from 2.636 V for $S = 4$ nm to 2.647 V for $S = 36$ nm. The results also show two different slopes for the plateau cell voltage versus nanostructure spacing curve. A more obvious increase in cell voltage with nanostructure spacing is observed for $S < 20$ nm (i.e., the pore-blocking regime where $S < 2\delta_{crit} = 25.4$ nm) due to the reduction of active surface area as a result of pore blocking. This is followed by a more subtle increase when $S > 26$ nm (i.e., the non-pore-blocking regime of $S > 2\delta_{crit}$) due to the slight increase in the specific area with nanostructure spacing.

Effect of structure height.—Figure 7 shows the simulated discharge profile and Li_2O_2 growth for electrodes of different nanostructure heights of H = 4, 10, 20, 50 nm while keeping the nanostructure spacing S = 30 nm. As shown in the cell voltage versus specific capacity plot in Figure 7a, an increase in nanostructure height results in both a greater cell voltage and a larger discharge capacity. When the nanostructure height increases from $H = 4$ to 50 nm, the plateau cell voltage increases from 2.637 to 2.685 V and the discharge capacity increases from 2399 to 5551 mAh g_c^{-1}.

In the kinetic-limited Li_2O_2 growth, the increase in electrode active surface area increases the cell voltage. In addition, because the nanostructure spacing is greater than twice the insulating thickness for all cases considered, pore blocking is avoided, which leads to an increase in specific capacity with electrode volume/mass. Figure 7c

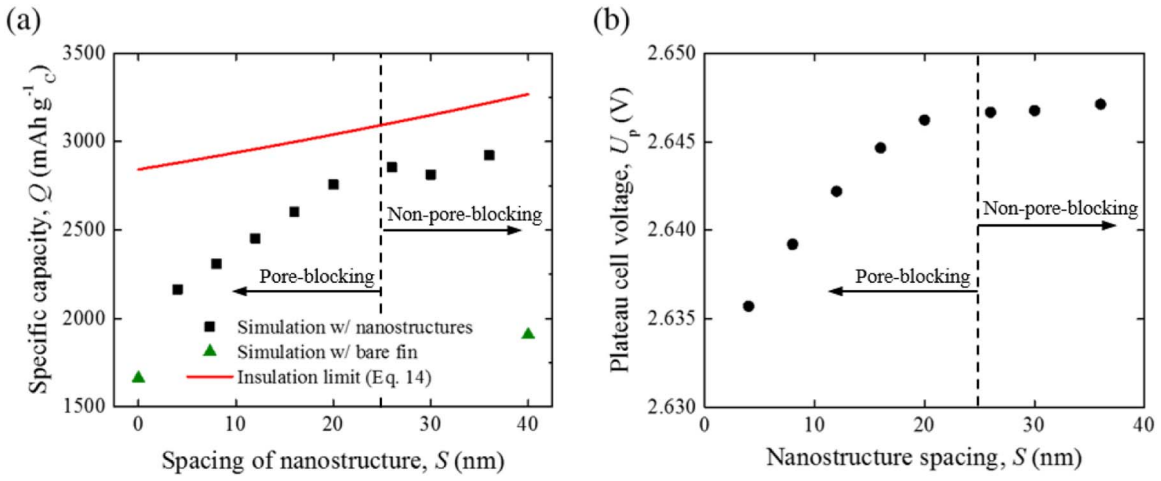

Fig. 6. (a) Comparison of simulated (symbols) and theoretical insulation limit (line) of specific discharge capacity as a function of nanostructure spacing. (b) Plateau cell voltage as a function of nanostructure spacing. The nanostructure spacing (S) and width (W) satisfy $S+W = 40$ nm and the specific area is held constant at 3.93 × 10^7 m^2/m^3.

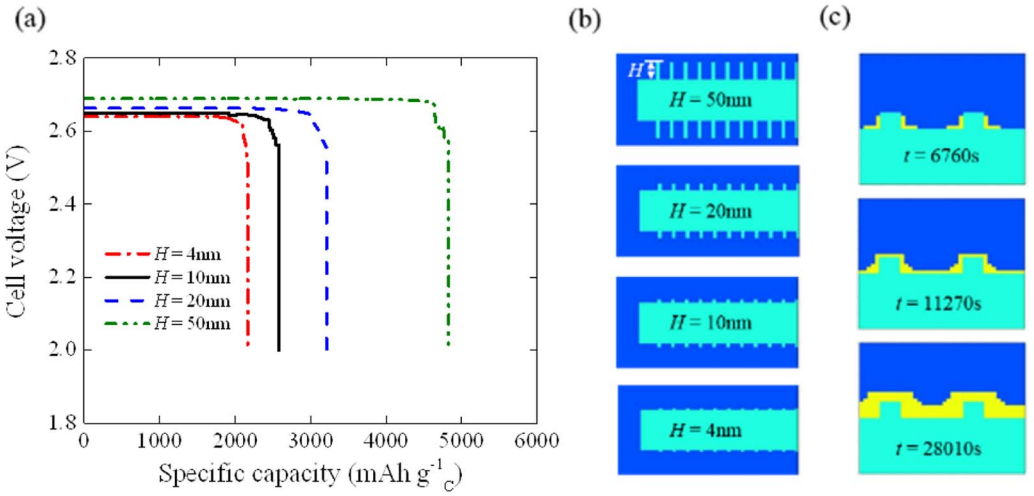

Fig. 7. (a) Discharge cell voltage as a function of specific capacity at different nanostructure heights. (b) Schematics of square nanostructured cathodes with different heights. (c) Zoomed-in snapshots (0.1 μm × 0.1 μm) of Li_2O_2 growth on electrode surface for the case with $S = 30$ nm and $H = 10$ nm. Snapshots are taken at the specific capacity of 475 mAh g_c^{-1}, 792 mAh g_c^{-1}, and 1968 mAh g_c^{-1}. The domain is a 0.64 μm × 0.58 μm periodic unit cell subject to galvanostatic discharge with a local current density of 2.5 mA m_c^{-2}.

shows a 0.1 μm × 0.1 μm section of the electrode to highlight the electrode structure and Li_2O_2 growth patterns for the $H = 10$ nm case at the specific capacity of 475 mAh g_c^{-1}, 792 mAh g_c^{-1}, and 1968 mAh g_c^{-1}. In the first frame, the onset of Li_2O_2 formation is observed at the concave corners of the electrode structure due to their higher local Li_2O_2 concentrations. Subsequent formation of the second and third frames shows that an entire monolayer of Li_2O_2 forms around the nanostructure before the growth of the next layer begins and the discharge process ends once the Li_2O_2 layer reaches the critical insulation thickness or the cell voltage drops below the discharge cutoff voltage of 2.0 V.

Conclusions

A pore-scale transport resolved model of the non-aqueous Li-air battery has been developed that is capable of simulating the species/charge transport and reaction kinetics at the distinct phases of liquid electrolyte, solid electrode, and lithium peroxide. This pore-scale approach is in contrast to the more common volume-averaged model, which considers the domain as a homogenous medium of uniform porosity. Utilizing a pore-scale approach requires no simplification or assumptions regarding the electrode morphology, and has enabled the detailed studies into the effects of the precise electrode microstructure. A model for the thickness-dependent Li_2O_2 conductivity is developed based on inputs from the DFT calculations and is incorporated into the pore-scale model to simulate the galvanostatic discharge of a nanostructured Li-air cell and validated by experiments. Good agreement is reached between the model and experiment, including the sudden drop in cell voltage at the end of discharge, which can not be recovered with the use of a constant Li_2O_2 conductivity. A critical insulation thickness of 12.6 nm for the Li_2O_2 buildup on the electrode surface is identified, above which the electrode becomes insulating.

The validated model is then used to examine the effects of the applied current density, the ORR rate coefficient, and the electrode geometry on cell performance. The results indicate that both the discharge voltage and capacity decrease with applied current density. The cell discharge capacity is limited by the spacing between nanostructures, which may lead to pore blocking and hence the reduction of active surface area. For the system considered, an increase in nanostructure spacing from 4 nm to 36 nm leads to a 35% increase in the specific discharge capacity. The height of nanostructures can also influence the specific discharge capacity, and both the discharge voltage and capacity increase with the nanostructure height as a result of increasing active area. By increasing the nanostructure height from 4 nm to 50 nm, the specific discharge capacity increases by approximately 120%.

The pore-scale model greatly benefits from the kinetic-limited Li_2O_2 growth mechanism, although the real growth mechanism may also depend upon the choice of electrolyte, discharge current, and catalyst. A forthcoming paper will extend the pore-scale model to three dimensions and examine the microstructural effects of digitally reconstructed electrodes, as well as the rate-dependent Li_2O_2 growth morphologies. The methodology presented here can be applied to any electrochemical system that includes an insoluble product formation as a result of the reaction process.

Acknowledgment

Support for this work was provided by the National Science Foundation (No. CBET-1318341). Computational resources were provided by the Extreme Science and Engineering Discovery Environment (XSEDE) (Grant #TG-CTS110056).

List of Symbols

A_s	Electrode specific area (m^2 g^{-1})
c	Species concentration (mol m^{-3})
D	Diffusion coefficient (m^2 s^{-1})
f	Activity coefficient
F	Faraday's constant (C mol^{-1})
H	Height of nanostructure (m)
$\mathbf{i}$	Electrolytic current density (mA m_c^{-2})
i_{ext}	External current density (mA m^{-2})
i_{local}	Local current density on cathode (mA m_c^{-2})
k_c	ORR rate coefficient (mol m^{-2} s^{-1})
L_x	Cathode x-direction length (m)
L_y	Cathode y-direction length (m)
M	Molecular weight (g mol^{-1})
$\mathbf{N}$	Butler-Volmer mass flux (mol m^{-2} s^{-1})
n	Number of electrons transferred in reaction
Q	Specific capacity (mAh g_c^{-1})
R	Universal gas constant (J mol^{-1} K^{-1})
S	Spacing of nanostructure (m)
s	Stoichiometric coefficient
T	Temperature (K)
t_+	Transference number

t	Time (s)
U_0	Open circuit voltage
U_p	Plateau cell voltage
W	Width of nanostructure (m)

Greek

β	Symmetry factor
Γ_{jk}	Interfacial boundary between subregions Ω_j & Ω_k
δ	Thickness of Li_2O_2 (m)
ε	Porosity, electrolyte volume fraction within the cell
η	Surface overpotential (V)
κ	Electrolytic conductivity (S m^{-1})
σ	Electrode or Li_2O_2 conductivity (S m^{-1})
ρ	Mass density (g m^{-3})
φ	Electric potential (V)
Ω	Simulation domain subregion (electrolyte, electrode, or Li_2O_2)
∇	Differential operator

Subscripts

0	Equilibrium value
b	Pore blocking
c	Carbon
crit	Critical value for insulation
ext	External value
f	End of discharge
i	Species $i \in \{O_2, Li^+, Li_2O_2\}$
ins	Cathode insulation
j	Subregion $j \in \{1, 2, 3\}$
local	Local value at cathode surface

Superscripts

0	Initial value
max	Maximum value

References

1. G. Girishkumar, B. McCloskey, A. C. Luntz, S. Swanson, and W. Wilcke, *Journal of Physical Chemistry Letters*, **1**, 2193 (2010).
2. M. S. Whittingham, *Chemical Reviews*, **104**, 4271 (2004).
3. J. E. Trevey, C. R. Stoldt, and S.-H. Lee, *Journal of The Electrochemical Society*, **158**, A1282 (2011).
4. X. L. Li and A. Faghri, *Journal of The Electrochemical Society*, **159**, A1747 (2012).
5. B. Richter, D. Goldston, G. Crabtree, L. Glicksman, D. Goldstein, D. Greene, D. Kammen, M. Levine, M. Lubell, and M. Savitz, *Energy Future: Think Efficiency*, in, American Physical Society, College Park, MD (2008).
6. J.-H. Lee, R. Black, G. Popov, E. Pomerantseva, F. Nan, G. A. Botton, and L. F. Nazar, *Energy & Environmental Science*, **5**, 9558 (2012).
7. S. A. Freunberger, Y. Chen, N. E. Drewett, L. J. Hardwick, F. Barde, and P. G. Bruce, *Angewandte Chemie*, **50**, 8609 (2011).
8. Y.-C. Lu, D. G. Kwabi, K. P. C. Yao, J. R. Harding, J. Zhou, L. Zuin, and Y. Shao-Horn, *Energy & Environmental Science*, **4**, 2999 (2011).
9. R. R. Mitchell, B. M. Gallant, C. V. Thompson, and Y. Shao-Horn, *Energy & Environmental Science*, **4**, 2952 (2011).
10. Z.-L. Wang, D. Xu, J.-J. Xu, L.-L. Zhang, and X.-B. Zhang, *Advanced Functional Materials*, **22**, 3699 (2012).
11. Y.-C. Lu, H. A. Gasteiger, M. C. Parent, V. Chiloyan, and Y. Shao-Horn, *Electrochemical and Solid State Letters*, **13**, A69 (2010).
12. B. M. Gallant, R. R. Mitchell, D. G. Kwabi, J. Zhou, L. Zuin, C. V. Thompson, and Y. Shao-Horn, *Journal of Physical Chemistry C*, **116**, 20800 (2012).
13. K. Mizushima, P. C. Jones, P. J. Wiseman, and J. B. Goodenough, *Materials Research Bulletin*, **15**, 783 (1980).
14. F. T. Wagner, B. Lakshmanan, and M. F. Mathias, *Journal of Physical Chemistry Letters*, **1**, 2204 (2010).
15. H.-G. Jung, J. Hassoun, J.-B. Park, Y.-K. Sun, and B. Scrosati, *Nature chemistry*, **4**, 579 (2012).
16. Z. Peng, S. A. Freunberger, Y. Chen, and P. G. Bruce, *Science*, **337**, 563 (2012).
17. Y. Zhang and C.-Y. Wang, *Journal of The Electrochemical Society*, **156**, A527 (2009).
18. J. S. Hummelshoj, J. Blomqvist, S. Datta, T. Vegge, J. Rossmeisl, K. S. Thygesen, A. C. Luntz, K. W. Jacobsen, and J. K. Norskov, *J Chem Phys*, **132** (2010).
19. S. P. Ong, Y. F. Mo, and G. Ceder, *Phys Rev B*, **85** (2012).
20. M. D. Radin, J. F. Rodriguez, F. Tian, and D. J. Siegel, *J Am Chem Soc*, **134**, 1093 (2012).
21. P. Albertus, G. Girishkumar, B. McCloskey, R. S. SaF́nchez-Carrera, B. Kozinsky, J. Christensen, and A. C. Luntz, *Journal of The Electrochemical Society*, **158**, A343 (2011).
22. V. Viswanathan, K. S. Thygesen, J. S. Hummelshoj, J. K. Norskov, G. Girishkumar, B. D. McCloskey, and A. C. Luntz, *J Chem Phys*, **135**, 214704 (2011).
23. B. D. McCloskey, D. S. Bethune, R. M. Shelby, G. Girishkumar, and A. C. Luntz, *Journal of Physical Chemistry Letters*, **2**, 1161 (2011).
24. S. A. Freunberger, Y. Chen, Z. Peng, J. M. Griffin, L. J. Hardwick, F. Barde, P. Novak, and P. G. Bruce, *Journal of the American Chemical Society*, **133**, 8040 (2011).
25. D. Aurbach, M. Daroux, P. Faguy, and E. Yeager, *J Electroanal Chem*, **297**, 225 (1991).
26. V. S. Bryantsev and M. Blanco, *Journal of Physical Chemistry Letters*, **2**, 379 (2011).
27. B. D. McCloskey, A. Speidel, R. Scheffler, D. C. Miller, V. Viswanathan, J. S. Hummelshøj, J. K. Nørskov, and A. C. Luntz, *The Journal of Physical Chemistry Letters*, **3**, 997 (2012).
28. M. W. Chase, Jr., *Journal of Physical and Chemical Reference Data*, Monograph 9 (1998).
29. Y. Shao, F. Ding, J. Xiao, J. Zhang, W. Xu, S. Park, J.-G. Zhang, Y. Wang, and J. Liu, *Advanced Functional Materials*, **23**, 987 (2013).
30. K. H. Xue, T. K. Nguyen, and A. A. Franco, *Journal of The Electrochemical Society*, **161**, E3028 (2014).
31. Y. Hu, X. Han, F. Cheng, Q. Zhao, Z. Hu, and J. Chen, *Nanoscale*, **6**, 177 (2014).
32. X.-h. Yang, P. He, and Y.-y. Xia, *Electrochemistry Communications*, **11**, 1127 (2009).
33. Y. Shen, D. Sun, L. Yu, W. Zhang, Y. Shang, H. Tang, J. Wu, A. Cao, and Y. Huang, *Carbon*, **62**, 288 (2013).
34. M. M. Ottakam Thotiyl, S. A. Freunberger, Z. Peng, Y. Chen, Z. Liu, and P. G. Bruce, *Nature Materials*, **12**, 1050 (2013).
35. C. Tran, X.-Q. Yang, and D. Qu, *Journal of Power Sources*, **195**, 2057 (2010).
36. P. Andrei, J. P. Zheng, M. Hendrickson, and E. J. Plichta, *Journal of The Electrochemical Society*, **157**, A1287 (2010).
37. U. Sahapatsombut, H. Cheng, and K. Scott, *Journal of Power Sources*, **227**, 243 (2013).
38. S. S. Sandhu, J. P. Fellner, and G. W. Brutchen, *Journal of Power Sources*, **164**, 365 (2007).
39. U. Sahapatsombut, H. Cheng, and K. Scott, *Journal of Power Sources*, **243**, 409 (2013).
40. Y. Wang, *Electrochimica Acta*, **75**, 239 (2012).
41. Y. Wang and S. C. Cho, *Journal of The Electrochemical Society*, **160**, A1847 (2013).
42. J. P. Zheng, R. Y. Liang, M. Hendrickson, and E. J. Plichta, *Journal of The Electrochemical Society*, **155**, A432 (2008).
43. A. Awarke, M. Wittler, S. Pischinger, and J. Bockstette, *Journal of The Electrochemical Society*, **159**, A798 (2012).
44. G. M. Goldin, A. M. Colclasure, A. H. Wiedemann, and R. J. Kee, *Electrochimica Acta*, **64**, 118 (2012).
45. G. B. Less, J. H. Seo, S. Han, A. M. Sastry, J. Zausch, A. Latz, S. Schmidt, C. Wieser, D. Kehrwald, and S. Fell, *Journal of The Electrochemical Society*, **159**, A697 (2012).
46. D. E. Stephenson, B. C. Walker, C. B. Skelton, E. P. Gorzkowski, D. J. Rowenhorst, and D. R. Wheeler, *Journal of The Electrochemical Society*, **158**, A781 (2011).
47. C.-W. Wang and A. M. Sastry, *Journal of The Electrochemical Society*, **154**, A1035 (2007).
48. P. Popov, Y. Vutov, S. Margenov, and O. Iliev, in *Numerical Methods and Applications*, I. Dimov, S. Dimova, and N. Kolkovska Editors, p. 338, Springer Berlin Heidelberg (2011).
49. G. Qiu, C. R. Dennison, K. W. Knehr, E. C. Kumbur, and Y. Sun, *Journal of Power Sources*, **219**, 223 (2012).
50. G. Qiu, A. S. Joshi, C. R. Dennison, K. W. Knehr, E. C. Kumbur, and Y. Sun, *Electrochimica Acta*, **64**, 46 (2012).
51. R. Black, S. H. Oh, J.-H. Lee, T. Yim, B. Adams, and L. F. Nazar, *Journal of the American Chemical Society*, **134**, 2902 (2012).
52. P. Andrei, J. P. Zheng, M. Hendrickson, and E. J. Plichta, *Journal of The Electrochemical Society*, **159**, A770 (2012).
53. S. S. Zhang, D. Foster, and J. Read, *Journal of Power Sources*, **195**, 1235 (2010).
54. B. M. Gallant, D. G. Kwabi, R. R. Mitchell, J. Zhou, C. V. Thompson, and Y. Shao-Horn, *Energy & Environmental Science*, **6**, 2518 (2013).
55. M. D. Radin and D. J. Siegel, *Energy & Environmental Science*, **6**, 2370 (2013).
56. J. Newman and K. E. Thomas-Alyea, *Electrochemical systems*, John Wiley & Sons (2012).
57. M. D. Radin, F. Tian, and D. J. Siegel, *Journal of Materials Science*, **47**, 7564 (2012).
58. J. Kang, Y. S. Jung, S. H. Wei, and A. C. Dillon, *Phys Rev B*, **85** (2012).
59. Y.-C. Lu, B. M. Gallant, D. G. Kwabi, J. R. Harding, R. R. Mitchell, M. S. Whittingham, and Y. Shao-Horn, *Energy & Environmental Science*, **6**, 750 (2013).
60. M. Bevilacqua, C. Bianchini, A. Marchionni, J. Filippi, A. Lavacchi, H. Miller, W. Oberhauser, F. Vizza, G. Granozzi, L. Artiglia, S. P. Annen, F. Krumeich, and H. Grützmacher, *Energy & Environmental Science*, **5**, 8608 (2012).

61. J.-J. Xu, Z.-L. Wang, D. Xu, L.-L. Zhang, and X.-B. Zhang, *Nat Commun*, **4** (2013).
62. B. D. Adams, C. Radtke, R. Black, M. L. Trudeau, K. Zaghib, and L. F. Nazar, *Energy & Environmental Science*, **6**, 1772 (2013).
63. J. Read, *Journal of The Electrochemical Society*, **149**, A1190 (2002).
64. C. Laoire, S. Mukerjee, E. J. Plichta, M. A. Hendrickson, and K. Abraham, *Journal of The Electrochemical Society*, **158**, A302 (2011).
65. B. D. McCloskey, D. S. Bethune, R. M. Shelby, T. Mori, R. Scheffler, A. Speidel, M. Sherwood, and A. C. Luntz, *The Journal of Physical Chemistry Letters*, **3**, 3043 (2012).
66. J. Read, K. Mutolo, M. Ervin, W. Behl, J. Wolfenstine, A. Driedger, and D. Foster, *Journal of The Electrochemical Society*, **150**, A1351 (2003).
67. B. Xie, H. S. Lee, H. Li, X. Q. Yang, J. McBreen, and L. Q. Chen, *Electrochemistry Communications*, **10**, 1195 (2008).
68. Y.-C. Lu and Y. Shao-Horn, *The Journal of Physical Chemistry Letters*, **4**, 93 (2013).
69. V. Y. Nimon, S. J. Visco, L. C. De Jonghe, Y. M. Volfkovich, and D. A. Bograchev, *ECS Electrochemistry Letters*, **2**, A33 (2013).
70. D. Xu, Z.-l. Wang, J.-j. Xu, L.-l. Zhang, and X.-b. Zhang, *Chemical Communications*, **48**, 6948 (2012).
71. O. Gerbig, R. Merkle, and J. Maier, *Advanced Materials*, **25**, 3129 (2013).
72. F. Tian, M. D. Radin, and D. J. Siegel, *Chem Mater*, **26**, 2952 (2014).
73. S. V. Patankar, *Numerical Heat Transfer and Fluid Flow*, Hemisphere Pub., Washington (1980).